




Article

Simulation of the Thermal Runaway Onset in Li-Ion Cells—Influence of Cathode Materials and Operating Conditions

Martina Cianciullo , Giorgio Vilardi, Barbara Mazzarotta  and Roberto Bubbico * 

Department of Chemical, Materials and Environmental Engineering, “Sapienza” University of Rome, Via Eudossiana 18, 00184 Rome, Italy; cianciullo.1755443@studenti.uniroma1.it (M.C.); giorgio.vilardi@uniroma1.it (G.V.); barbara.mazzarotta@uniroma1.it (B.M.)

* Correspondence: roberto.bubbico@uniroma1.it; Tel.: +39-06-44585780

Abstract: Li-ion batteries are already being used in several applications, from portable devices to the automotive industry, and they represent a promising option also for other critical uses, such as in the storage of energy from renewable sources. However, two of the main concerns that still hinder their massive introduction in these further areas, are their safety and reliability. Depending on cell characteristics and operating conditions, the heat generated within the cell can exceed that dissipated from its surface, and the cell will fail, possibly with catastrophic consequences. To identify the hazardous working conditions of a cell, a simulation model including the main exothermic reactions was set up to investigate the onset of thermal runaway in several Li-ion cell configurations under various operating conditions. The behavior of four different cathodes under thermal abuse and the influence of external factors such as the environmental temperature and the cooling system efficiency were assessed. It was found that among those investigated, the lithium iron phosphate cathode is characterized by a higher thermal stability and that an efficient superficial heat exchange can prevent thermal runaway in most of the cases.

Keywords: Li-ion batteries; energy storage; battery safety; thermal runaway



Citation: Cianciullo, M.; Vilardi, G.; Mazzarotta, B.; Bubbico, R. Simulation of the Thermal Runaway Onset in Li-Ion Cells—Influence of Cathode Materials and Operating Conditions. *Energies* **2022**, *15*, 4169. <https://doi.org/10.3390/en15114169>

Academic Editor: Xia Lu

Received: 11 May 2022

Accepted: 1 June 2022

Published: 6 June 2022

Publisher’s Note: MDPI stays neutral with regard to jurisdictional claims in published maps and institutional affiliations.



Copyright: © 2022 by the authors. Licensee MDPI, Basel, Switzerland. This article is an open access article distributed under the terms and conditions of the Creative Commons Attribution (CC BY) license (<https://creativecommons.org/licenses/by/4.0/>).

1. Introduction

Nowadays, Li-ion batteries are commonly applied in a wide range of applications, from mobile devices (cell phones, laptops, etc.), to automotive (electric and hybrid electric vehicles) and even larger stationary applications in the power industry [1–4], where continuously increasing energy densities need to be stored. However, in order to allow a more stable and widespread use of these batteries, especially in critical applications requiring high levels of safety and reliability, some critical issues need still be addressed, most of them being associated with the occurrence of thermal runaway [5–10]. This phenomenon is associated with the internal generation of heat, due to a variety of exothermic reactions occurring within the cell, especially under abuse conditions (overcharge/overdischarge, thermal or mechanical abuse, and others). When this heat is not adequately dissipated toward the exterior of the cell, it causes an internal temperature rise and thus the acceleration of the exothermic reactions themselves or the ignition of additional reactions, with further uncontrolled overheating. This will finally lead to the failure of the cell, often catastrophic, with the generation of fires and explosions and the possible involvement of additional cells in a pack with even more severe consequences [7,11–14].

The identification of these hazardous conditions [7–10,15–17] is of the utmost importance to prevent the occurrence of thermal runaway and to design adequate protection systems and devices (PTC, BMS, etc.), thus allowing to prevent accidents or power shut-downs [13,18–27]. However, an efficient analysis requires detailed knowledge of the dynamic phenomena involved in the thermal runaway onset and its development.

The main components of a Li-ion battery are the cathode, the anode, and the electrolyte. At present, in most practical applications, the anode consists almost exclusively of graphite; the cathode usually contains a metal oxide, such as lithium cobalt oxide LiCoO_2 , lithium manganese oxide LiMn_2O_4 , and lithium iron phosphate LiFePO_4 , and the electrolyte is usually based on a solvent containing a mixture of organic carbonates (mainly ethylene carbonate EC, diethyl carbonate DEC, and dimethyl carbonate DMC). However, there is a continuous search for better-performing and safer materials, so a wider combination of components is possible, making a generalized analysis more complex [28–31].

In order to have better knowledge of the failure modes of a Li-ion cell, both experimental and theoretical analyses have been carried out in the literature. Due to the difficulties of performing an extended experimental investigation, especially on a large scale, only a few field data are available in the literature [32–40], often referred to a limited number of system configurations (cell size, components, operating, and abuse conditions, and so on), or to the assessment of specific parameters [41–47].

A larger number of papers report theoretical analyses; however, due to the complexities of a rigorous mathematical representation of the system, several simplifying hypotheses are often introduced to make the calculation effort more reasonable [11,48–53].

It is generally recognized that most of the heat produced during thermal runaway is caused by the decomposition of the solid electrolyte interface (SEI), by reactions between the electrodes (anode and cathode) and the electrolyte, by the electrolyte decomposition, and by some other phenomena [11,54–59].

In the present paper, several configurations of cylindrical Li-ion cells subjected to abuse conditions of high current were analyzed, and their behavior was compared in terms of safe operational range, maximum temperature reached at a steady state, and operation time before the start of thermal runaway, as a function of operating conditions. In particular, four different cathodes were simulated, namely LiMn_2O_4 (LMO), LiFePO_4 (LFP), $\text{LiNi}_{0.4}\text{Co}_{0.2}\text{Mn}_{0.4}\text{O}_2$ (NMC), and LiCoO_2 (LCO), while graphite and LiPF_6 lithium salt in 1:1 EC:EMC solvent were always assumed as anode and electrolyte, respectively. Each cell was simulated under continuous cycles of charge/discharge phases at 80 A/m^2 and exposed to varying external cooling conditions. Unlike most previous studies, the physical properties of the materials involved were considered as a function of the changing temperature over time but were assumed constant in space. In addition, the direct comparison of several combinations of materials and external conditions, rather than focusing on single configurations, allowed to derive more clear conclusions in terms of thermal stability and safety of the cells.

The results allow to identify the optimal operating conditions to avoid a thermal runaway for each cell type, and their general trend can reasonably be extended to other configurations/materials, although the absolute values of the parameters involved (air temperature, flow rate, etc.) still need to be experimentally assessed. In addition to the analysis of single cells with different chemical characteristics, the case of a cell exposed to an external heat flux due to other neighboring cells experiencing a thermal runaway in a battery pack was also investigated.

2. Model Overview

Given the variety of interacting phenomena involved in the operation of a Li-ion cell, its modeling requires both a multiphysics and multiscale approach, and although this is already a simplified approach, it is still computationally demanding. In this paper, the model was implemented in COMSOL Multiphysics v5.5 [60,61], where both the electrochemical and the thermal processes were simultaneously represented making use of the *Battery and Fuel Cell* module. Additional information on modeling and a critical comparison of models can be found in the useful literature reviews [62].

The electrochemical model is based on the theory of the porous electrode: the current flows both in the solid electrode and across its pores containing the electrolyte. The equations required to describe this system are the materials balance in the solid and in

the electrolyte, the charge conservation within the solid and the pores, and the kinetic reactions equations. The separator will be described by the materials balance and charge conservation for the liquid phase.

The transport of the Li particles within the electrode during charge and discharge is described by the Fick's law in spherical form [63–65],

$$\frac{\partial c_{s,i}}{\partial t} = \frac{D_s}{r^2} \frac{\partial}{\partial r} \left(r^2 \frac{\partial c_s}{\partial r} \right) \quad (1)$$

with c_s [mol/m³] and D_s [m²/s] as the lithium concentration and diffusivity, respectively.

At the particle center and on its external surface (particle radius R_p , [m]), the conditions of no flow and of local current density will apply:

$$\left. \frac{\partial c_{s,i}}{\partial r} \right|_{r=0} = 0 \quad (2)$$

$$-D_{s,i} \left. \frac{\partial c_{s,i}}{\partial r} \right|_{r=R_p} = \frac{i_{loc}}{F} \quad (3)$$

The transport of Li-ions within the electrolyte is governed by Fick's diffusion law and electromigration. In addition, according to the electroneutrality assumption [66], it can be written as:

$$\frac{\partial c_1 \epsilon_1}{\partial t} = \nabla (D_{l,eff} \nabla c_1) + a_s \frac{(1 - t_+)}{F} i_{loc} \quad (4)$$

with c_1 [mol/m³] as the concentration of Li-ions within the electrolyte; ϵ_1 is the volume fraction of the electrolyte; a_s is the specific interface area (cm²/cm³); i_{loc} is the local current density at the electrode (A/cm²), and t_+ is the transference number of Li-ions with respect to the velocity of the solvent (–). The diffusion coefficient $D_{l,eff}$ is derived from the Bruggeman relation:

$$D_{l,eff} = \epsilon_{l,i}^b D_l \quad (5)$$

with the Bruggeman factor b usually equal to 1.5.

The boundary conditions represent a null flux, corresponding to no ion penetration at the interface of the current collectors, on the metal, on the external surfaces, and on the symmetry axis at $r = 0$:

$$\left. \frac{\partial c_1}{\partial r} \right|_{r=0} = 0 \quad (6)$$

$$\left. \frac{\partial c_1}{\partial r} \right|_{r=R_p} = 0 \quad (7)$$

$$\left. \frac{\partial c_1}{\partial z} \right|_{z=L_{as}} = \left. \frac{\partial c_1}{\partial z} \right|_{z=L_{sc}} = 0 \quad (8)$$

$$\left. \frac{\partial c_1}{\partial z} \right|_{z=L_{ca}} = \left. \frac{\partial c_1}{\partial z} \right|_{z=L_{cc}} = 0 \quad (9)$$

$$\left. \frac{\partial c_1}{\partial r} \right|_{r=R_m} = 0 \quad (10)$$

Charge conservation within the solid electrode is governed by the equation

$$\nabla i_s = -a_s i_{loc} \quad (11)$$

where a_s is the specific interfacial area characterizing the electrode

$$a_s = \frac{3\epsilon_s}{R_p} \quad (12)$$

with i_s as the current density in the solid phase, given by an Ohm expression:

$$i_s = -\sigma_{s,\text{eff}} \nabla \phi_s \quad (13)$$

In the above equation, ϕ_s [V] is the potential at the electrodes, and $\sigma_{s,\text{eff}}$ is the effective electric conductivity in the solid phase, which depends on the electric conductivity of the material and its porosity, according to the Bruggeman relation:

$$\sigma_{s,\text{eff}} = \epsilon_{s,i}^b \sigma_s \quad (14)$$

A no-current condition is applied at the SEI

$$\frac{\partial \phi_s}{\partial z} \Big|_{z=L_{\text{as}}} = \frac{\partial \phi_s}{\partial z} \Big|_{z=L_{\text{sc}}} = 0 \quad (15)$$

while a symmetry condition for the potential of the solid phase for $r = 0$ and an isolation condition at the external surface of the electrode solid phase apply:

$$\frac{\partial \phi_s}{\partial r} \Big|_{r=0} = 0 \quad (16)$$

$$\frac{\partial \phi_s}{\partial r} \Big|_{r=R_p} = 0 \quad (17)$$

Within the electrolyte, the current flow is due to the Li-ion migration and diffusion

$$i_1 = -\sigma_{1,\text{eff}} \nabla \phi_1 + \left(\frac{2\sigma_{1,\text{eff}} RT}{F} \right) \left(1 + \frac{\partial \ln f}{\partial \ln c_1} \right) (1 - t_+) \nabla \ln c_1 \quad (18)$$

where ϕ_1 [V] is the electrolyte potential; f represents the average molar coefficient of activity, which results in a concentration gradient due to the effect of the polarization potential, and $(1 + \partial \ln f / \partial \ln c_1)$ is a thermodynamic factor.

A symmetry condition also applies for $r = 0$, and a null flux condition at the electrode-collector interface and on the external surface of the electrode separator.

$$\frac{\partial \phi_s}{\partial r} \Big|_{r=0} = 0 \quad (19)$$

$$\frac{\partial \phi_1}{\partial z} \Big|_{z=L_{\text{ca}}} = \frac{\partial \phi_1}{\partial z} \Big|_{z=L_{\text{cc}}} = 0 \quad (20)$$

The kinetics for the electrochemical reactions are represented by a Butler–Volmer equation, providing the following equation for the current density:

$$i_{\text{loc},m} = i_0 \left(\exp \left(\frac{\alpha_0 F \eta}{RT} \right) - \exp \left(\frac{-\alpha_c F \eta}{RT} \right) \right) \quad (21)$$

where i_0 is the exchanged current density; α_0 the anodic transfer coefficient; α_c is the cathodic transfer coefficient; F is the Faraday constant; T is the absolute temperature; R is the universal gas constant, and η is the overcharge:

$$\eta_m = \phi_s - \phi_1 - E_{\text{eq},m} \quad (22)$$

$E_{\text{eq},m}$ depends both on the temperature and on the state of charge of the cell:

$$E_{\text{eq},m} = E_{\text{eq},i} + \frac{\partial U_{\text{eq},i}}{\partial T} (T - T_{\text{ref}}) \quad (23)$$

The current density is thus calculated as

$$i_0 = Fk_0(c_l)^{\alpha_0}(c_{s,\max} - c_s)^{\alpha_a}(c_s)^{\alpha_c} \quad (24)$$

With k_0 as the kinetic constant and $c_{s,\max}$ as the maximum Li concentration in the solid phase.

As far as the energy balance of the cell is concerned, it must be observed that heat generation inside the cell originates from three different sources: (1) heat generated by entropy variations during charge/discharge cycles, usually referred to as entropic reversible heat $q_{\text{rev}} = a_s i_{\text{loc}} T (\partial U_{\text{eq}} / \partial T)$; (2) heat generated by irreversible electrochemical reactions, $q_{\text{irr}} = a_s i_{\text{loc}} \eta$; and (3) heat generated by electron transfer in the solid phase and by Li-ion migration and diffusion within the electrolyte. The latter term, often denoted as Ohmic heat q_{ohm} , is usually split into three different components: electric Ohmic heat $q_{\text{ohm},s}$, ionic Ohmic heat $q_{\text{ohm},i}$, and Ohmic heat due to an internal short circuit in the metal or the collector $q_{\text{ohm},m}$.

The resulting overall balance equation is given by:

$$\rho c_p \frac{\partial T}{\partial t} = k \nabla^2 T + q_{\text{rev}} + q_{\text{irr}} + q_{\text{ohm}} \quad (25)$$

3. Simulation Implementation

In order to optimize the calculation burden [40,49,63,67–74], the whole model was set up using two different geometries connected to each other to exchange the required information. One-dimensional geometry was used to characterize the basic chemical reactions of the specific type of cell (LCO, LMO, NMC, or LFP), and it ran in all simulations. Two-dimensional geometry was needed to simulate the thermal behavior of the cell; at each incremental step, it provided the temperature variations to the 1D component and then retrieved the physical properties calculated by the 1D geometry at the updated T.

3.1. One-Dimensional Component

The one-dimensional component handles the chemical characteristics of the cell, and to this end, use was made of the physical interface *Lithium Ion Battery* present in COMSOL Multiphysics. Three options associated with this interface were adopted to represent the different issues of the model:

- *Porous Electrode* to define the charge balance for the electrodes and the electrolyte inside the pores;
- *Porous Electrode Reaction* to define the charge transfer reactions at the interface between the electrodes and the electrolytes;
- *Separator* to represent the separator properties (conductivity, diffusivity, etc.).

The geometrical dimensions of the one-dimensional component were assumed in accordance with previous analyses from the literature [75–78], and they are reported in Table 1.

Table 1. Cell's component size.

L_anode	55 μm	Negative electrode thickness
L_separator	30 μm	Separator thickness
L_cathode	55 μm	Positive electrode thickness
L_cc_negative	7 μm	Negative collector thickness
L_cc_positive	10 μm	Positive collector thickness
L_cell ¹	157 μm	Cell thickness

¹ L_cell = L_anode + L_separator + L_cathode + L_cc_negative + L_cc_positive.

As far as the chemical characterization of the cells is concerned, the main properties of the four cathodes adopted for the simulations were already present in the COMSOL library. Each cell was simulated for continuous cycles of charge/discharge phases, with a duration of 500 s for each full cycle, at a constant current of $i = \pm 80 \text{ A/m}^2$, without any relaxation time (Figure 1).

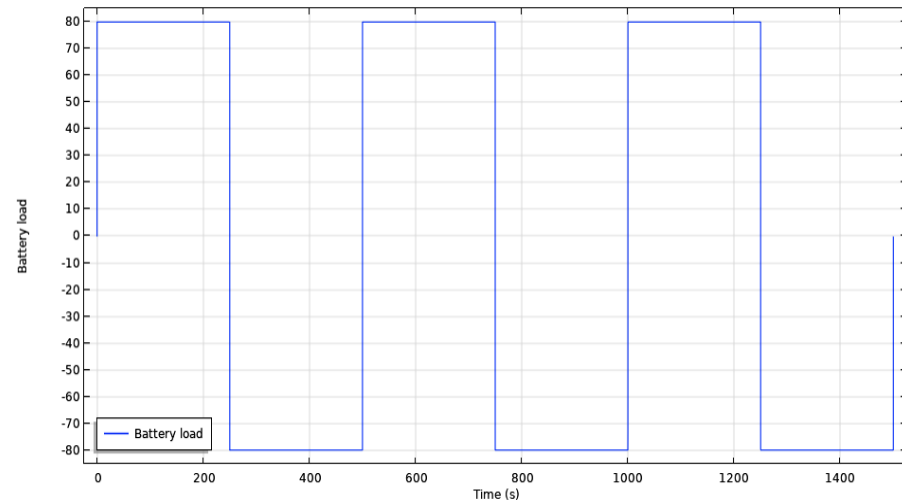


Figure 1. Battery load vs. time.

3.2. Two-Dimensional Component

The two-dimensional component was used to represent the internal heat generation. The main items setting up a whole cylindrical cell are: (a) the mandrel, a low conductivity material supporting the active layers; (b) the external metal protective can; and (c) the internal active materials. The latter item consists of a series of alternating layers of cathode, anode, separator, etc. spirally wound around the mandrel. In order to simplify the calculations, the various active layers of a real cell were modeled as a single pseudo-homogeneous active material with constant average properties. This also allows the adoption of an axial symmetry on an x - y plane with respect to $x = 0$, as represented in Figure 2, where the main components of the cell are shown; their corresponding dimensions are reported in Table 2, while their physical properties are reported in Table 3 [75–78].

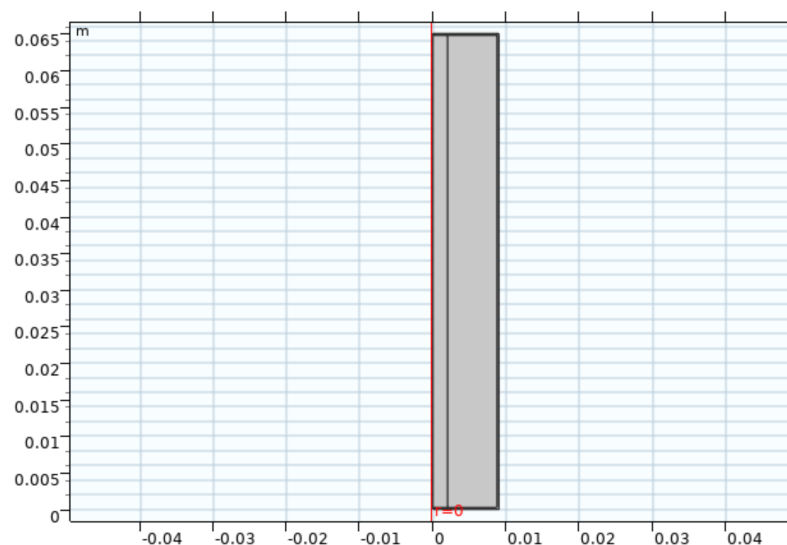


Figure 2. Two-dimensional axial-symmetric geometry.

Table 2. Two-dimensional cell component size.

r_{cell} [m]	9×10^{-3}	Cell radius
h_{cell} [m]	6.5×10^{-2}	Cell height
r_{mandrel} [m]	2×10^{-3}	Mandrel radius
$r_{\text{connector}}$ [m]	3×10^{-3}	Connector radius
$h_{\text{connector}}$ [m]	3×10^{-3}	Connector height
d_{can} [m]	0.25×10^{-3}	External can thickness

Table 3. Physical properties of cell's materials.

Material	k [W/mK]	c_p [J/kgK]	ρ [kg/m ³]	Source
Copper	298.15	385	8933	[75]
Aluminum	170	875	2770	[75]
Separator	0.344	1978	1009	[75]
Graphite	1.04	1437	1347	[75]
LCO	1.48	700	2500	[77]
LMO	1.58	1269	2329	[60]
NMC	3.4	1000	2500	[60]
LFP	1.48	1260	1500	[77]

Given the structure of the active material, the thermal conductivity is anisotropic, and its radial and axial values can be derived by the following equations, respectively [11,77]:

$$k_{T,r} = \frac{\sum L_i}{\sum \frac{L_i}{k_{T,i}}} \quad (26)$$

and

$$k_{T,a} = \frac{\sum L_i k_{T,i}}{\sum L_i} \quad (27)$$

where L_i and $k_{T,i}$ are the thickness and the thermal conductivity of the single layers composing the active element.

Similarly, the average heat capacity and density were calculated as

$$\rho_a = \frac{\sum L_i \rho_i}{\sum L_i} \quad (28)$$

and

$$c_{p,a} = \frac{\sum L_i c_{p,i}}{\sum L_i} \quad (29)$$

The mandrel and the external were assumed to be composed of nylon and steel, respectively.

The physical interface *Heat Transfer in Solids* present in COMSOL was adopted to introduce the heat sources in the model. The heat generated by the Joule effect in the active material ($Q_{h,3D}$ [W/m³]) was based on the results obtained by the 1D model and integrated in the whole cell volume

$$Q_{h,3D} = Q_{h,1D} \frac{L_{\text{an}} + L_{\text{sep}} + L_{\text{cat}}}{L_{\text{cell}}} \frac{\left((r_{\text{cell}} - d_{\text{can}})^2 - r_{\text{mandrel}}^2 \right) (h_{\text{cell}} - 2d_{\text{can}})}{(r_{\text{cell}}^2 - r_{\text{mandrel}}^2) h_{\text{cell}}} \quad (30)$$

The temperature distribution calculated by the 2D model was then recycled to the 1D model to update it and recalculate the generated heat and all other temperature-dependent parameters in a continuous circular exchange of information. Unlike most of the previous papers, all physical parameters here were calculated as a function of the variable temperature.

The other source of heat generation was associated with the exothermic reactions, which gradually occurred with increasing temperature, and were conventionally grouped in the following four categories [11,75–78]:

- SEI decomposition in the range between 90 and 120 °C;
- Reactions between anode and electrolyte at $T > 120$ °C;
- Reactions between cathode and electrolyte at $T > 170$ °C;
- Electrolyte decomposition at $T > 200$ °C.

The common approach of introducing an average value of the heat generated by the many, and often interacting, exothermic reactions [11,75–78] was also adopted here, and the specific values of the involved parameters are presented below.

The total exothermic heat was calculated as the sum of all the above contributions:

$$Q = Q_{\text{SEI}} + Q_{\text{anode}} + Q_{\text{cathode}} + Q_{\text{electrolyte}} \quad (31)$$

where for each of the above terms, an Arrhenius-like kinetics was assumed [11,32,39,77]

$$Q_i(x, t) = q_i R_i(x, t) \quad (32)$$

$$R_i(x, t) = A_i c_i^{m_i}(x, t) \exp\left(-\frac{E_{a,i}}{RT(x, t)}\right) \quad (33)$$

Adopting the Constant Fuel Model, the dependence on time and space can be neglected [79], and m_i can be assumed as 1, so that the concentration will only depend on the temperature

$$c_i(x, t) = c_{i,0}, \quad |t > 0, \quad x \in \Omega_i \quad (34)$$

Ω_i represents the whole volume where the exothermic reactions occur.

The resulting equation for each exothermic reaction heat is thus:

$$Q_i(x, t) = q_i A_i c_{i,0} \exp\left(-\frac{E_{a,i}}{RT(x, t)}\right) \quad (35)$$

and the values of the kinetic parameters used in the simulations are reported in Table 4.

Table 4. Parameters for kinetic Equation (35) [54,75,77].

	Heat of Reaction q_i [$\frac{\text{J}}{\text{kg}}$]	Frequency Factor A_x [$\frac{1}{\text{s}}$]	Activation Energy E_A [$\frac{\text{J}}{\text{mol}}$]	Volume W_y [$\frac{\text{kg}}{\text{m}^3}$]	Nondimensional Concentration $c_{i,0}$
SEI decomposition	2.57×10^5	1.667×10^{15}	1.3508×10^5	1.39×10^3	0.15
Anode reactions	1.714×10^6	2.5×10^{13}	1.3508×10^5	1.39×10^3	0.75
Cathode reactions	3.14×10^5	6.667×10^{13}	1.396×10^5	1.3×10^3	0.0384
Electrolyte decomposition	1.55×10^5	5.14×10^{25}	2.74×10^5	5×10^2	1

4. Model Results and Discussion

4.1. Single Cells

The results obtained by applying the present model to different single cells under several operating conditions are presented below. The model was preliminarily validated against the literature data comparing the trend of the thermal runaway ignition time (t_{TR}) for different external heat exchange coefficients and different ambient/initial temperatures, adopting the LCO cathode configuration (Figure 3). It is apparent from Figure 3 that the agreement is quite good.

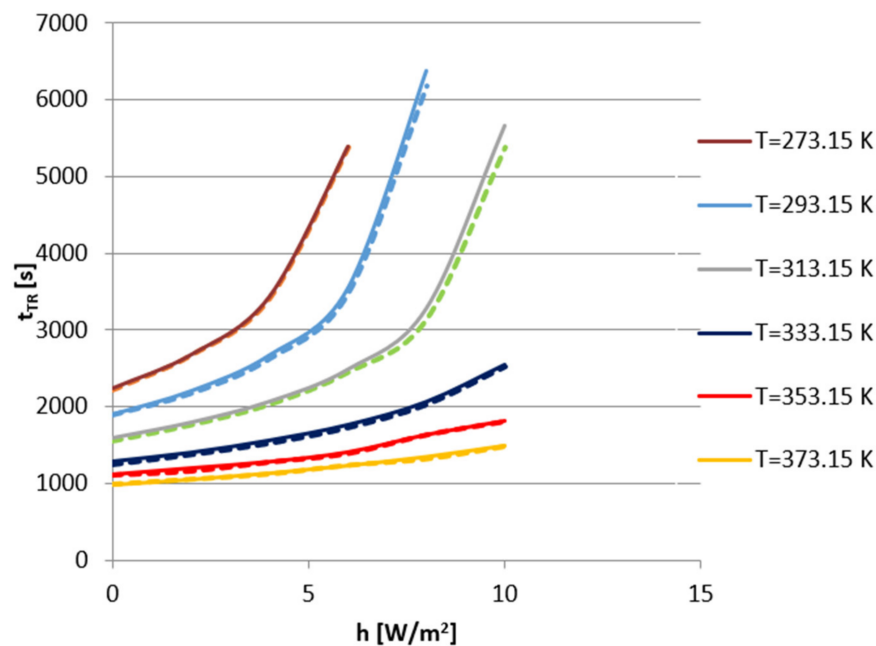


Figure 3. Thermal runaway ignition time (t_{TR}) as a function of h and ambient temperature for the LCO cathode. Solid lines = literature data [75]; dashed lines = present model results.

The results are also reported in Table 5 for the sake of completeness. As might be expected, the thermal runaway ignition time markedly increases at higher heat transfer coefficients (higher thermal stability of the cell), while it decreases at higher initial temperatures, also because of a reduced cooling effect by the warmer external environment.

Table 5. Ignition time (s) at different h (W/m^2K) and ambient temperatures.

T_{env} (K)	h (W/m^2K)	0	2	4	6	8	10
273.15 K		2213	2665	3408	5374		
293.15 K		1892	2172	2624	3476	6179	
313.15 K		1550	1760	2026	2445	3137	5379
333.15 K		1252	1378	1525	1727	2024	2513
353.15 K		1113	1163	1278	1388	1627	1798
373.15 K		983	1047	1115	1229	1311	1474

In order to clearly highlight the influence of the exothermic reactions on the cell temperature, reference simulations were preliminarily carried out neglecting those reactions. Figures 4–7 show the trend of the internal temperature as a function of time, for the LCO, LMO, NMC, and LFP configurations, respectively, with values of the external heat transfer coefficients in the range of 0–20 W/m^2K , which correspond to typical stationary or low-velocity flow of gases or air (natural convection) [77,80,81] in the cooling system.

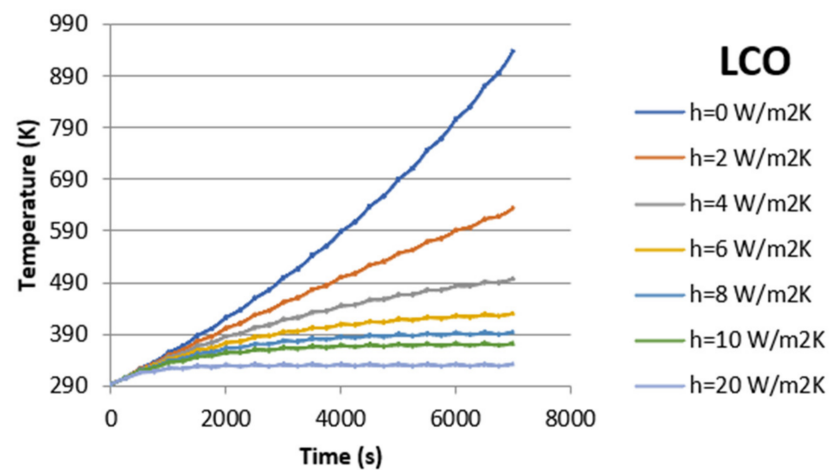


Figure 4. Temperature profile for an LCO cell in the absence of exothermic reactions.

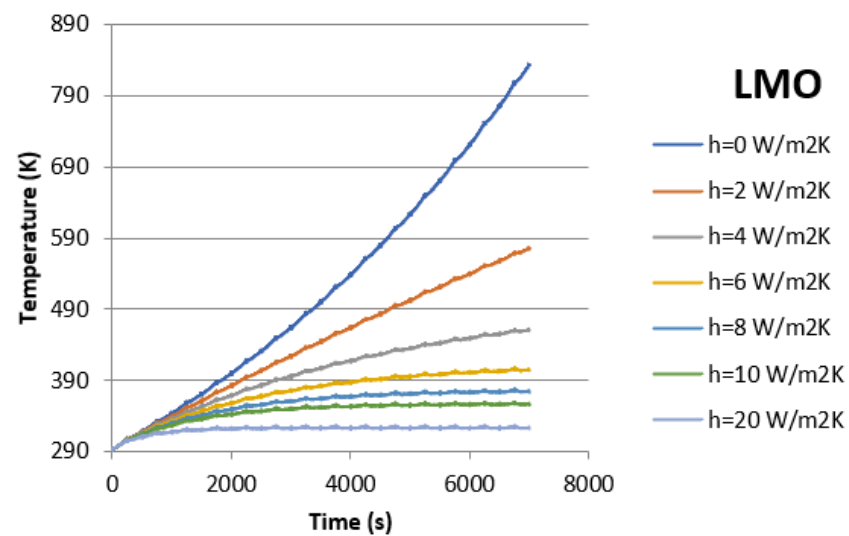


Figure 5. Temperature profile for an LMO cell in the absence of exothermic reactions.

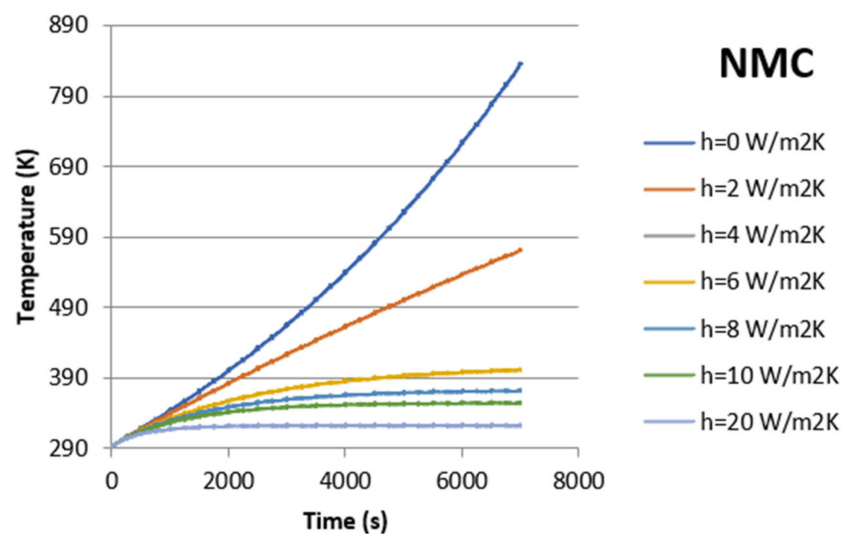


Figure 6. Temperature profile for an NMC cell in the absence of exothermic reactions.

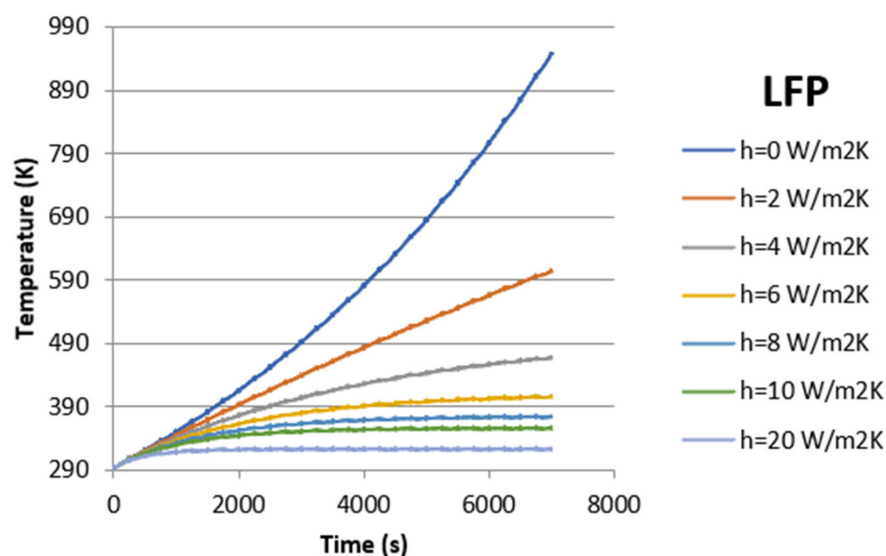


Figure 7. Temperature profile for an LFP cell in the absence of exothermic reactions.

It can be seen that, as expected, a more or less pronounced continuous increase in the temperature with time was calculated, depending on the heat dissipation capacity of the cell; however, in all cases the cell operates for a relatively long-time interval, without experiencing thermal runaway. In particular, with high enough heat exchange coefficients, the cell temperature initially rises, but after some time (in the order of several hours), it reaches a stable value for the rest of the cell operation.

If the exothermic reactions are included in the model, a different behavior of the cell temperature is obtained: depending on the cell type and operating conditions, at a given time, a sudden dramatic increase in the temperature is observed, corresponding to the thermal runaway ignition.

In the following Figures 8–13, the time profile of the cell temperature at different values of the heat transfer coefficient ($h = 0\text{--}10\text{ W/m}^2\text{K}$) is reported; on each graph, the results for all the cathodes are shown to allow an easier comparison among them. In all cases, an initial ambient temperature of 293 K was assumed. As a general observation, the cell temperature almost linearly increases for some time until it reaches the ignition temperature of the thermal runaway, when the heat production cannot be controlled any longer by the external heat exchange, and the failure of the cell will occur [78]. For all cell types, this will happen earlier for lower heat exchange coefficients, with minimum values under adiabatic conditions ($h = 0\text{ W/m}^2\text{K}$), while for higher values of h , longer operation times can be obtained; in particular, for $h = 10\text{ W/m}^2\text{K}$, the produced heat is always adequately dissipated from the cell surface, and thermal runaway is prevented (Figure 13). This result confirms and extends to a larger number of chemistries the results reported by Melcher et al. [75] and Lopez et al. [77] for LCO cells. In the case of the LFP cell, this favorable condition was established already for $h = 8\text{ W/m}^2\text{K}$, even though reaching a final temperature of 357 K vs. 347 K for $h = 10\text{ W/m}^2\text{K}$. The latter considerations denote a reduced susceptibility of the LFP type of chemistry to runaway conditions with respect to the other ones. Conversely, from this point of view, the LCO cathode cell is always more prone to runaway conditions, with the ignition time for thermal runaway always lower and often much lower than those found for the other cathodes (often nearly half those for LFP). Similar to the present results and based on oven tests, Fouchard et al. [82] observed that LiMn_2O_4 cathodes offer better thermal stability than LiCoO_2 or LiNiO_2 cathodes. After the accelerating rate calorimetry (ARC) measurements on 18,650 Li-ion cells at different state of charges (SOCs), Mendoza-Hernandez et al. [83] found that LMO cells presented a higher thermal stability than LCO cells and also put forward the hypothesis that this might be due to the higher amount of oxygen possibly released by the latter cathode and thus available for combustion reactions. Using ARC data, Jiang and Dahn [84] also detected

a much higher thermal stability of the LiFePO_4 cathode, compared to the LiCoO_2 and $\text{Li}[\text{Ni}_{0.1}\text{Co}_{0.8}\text{Mn}_{0.1}]\text{O}_2$ cathodes, especially in a LiBoB EC/DEC electrolyte.

Limiting the analysis to the conditions where a linear temperature increase is calculated (i.e., approximately up to $h = 6 \text{ W/m}^2\text{K}$), Figure 14 shows the overall influence of h on cell heating. As already mentioned, LCO cells always show a higher absolute value of the temperature rise (dT/dt) at any h , but the influence of a variation of h is very similar for all chemistries, as represented by the almost equal slopes of the fitting lines for the different cathodes.

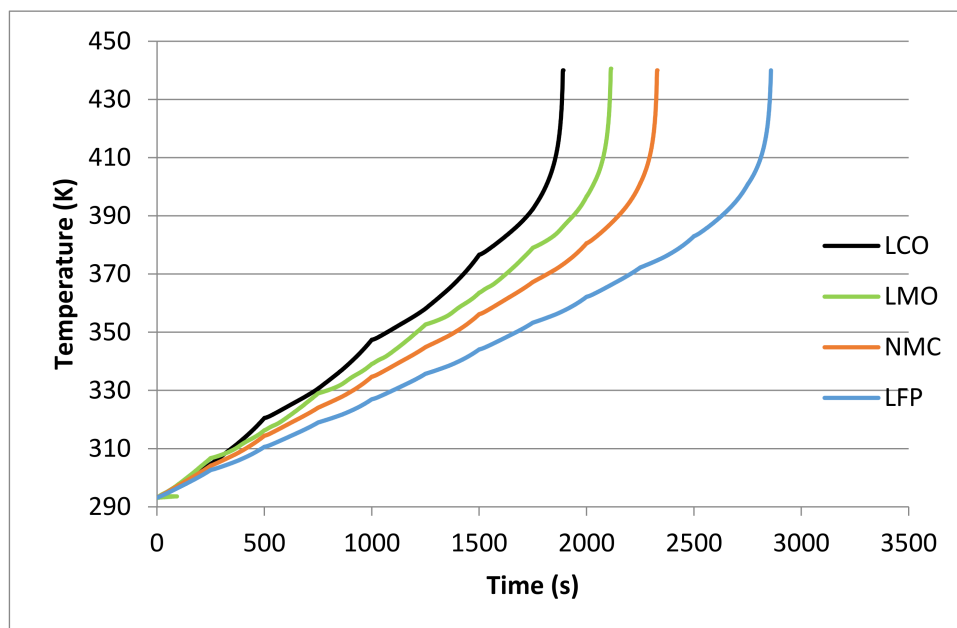


Figure 8. Temperature profiles as a function of time ($h = 0 \text{ W/m}^2\text{K}$).

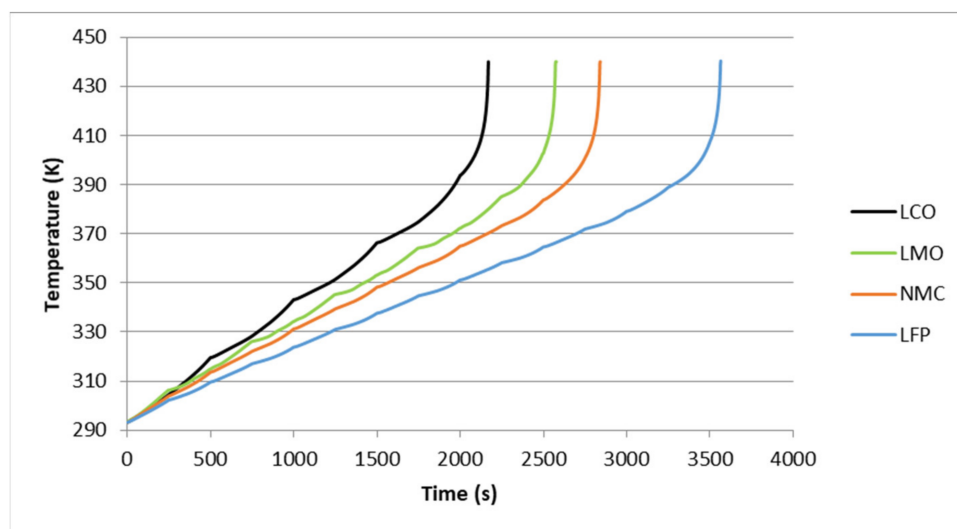


Figure 9. Temperature profiles as a function of time ($h = 2 \text{ W/m}^2\text{K}$).

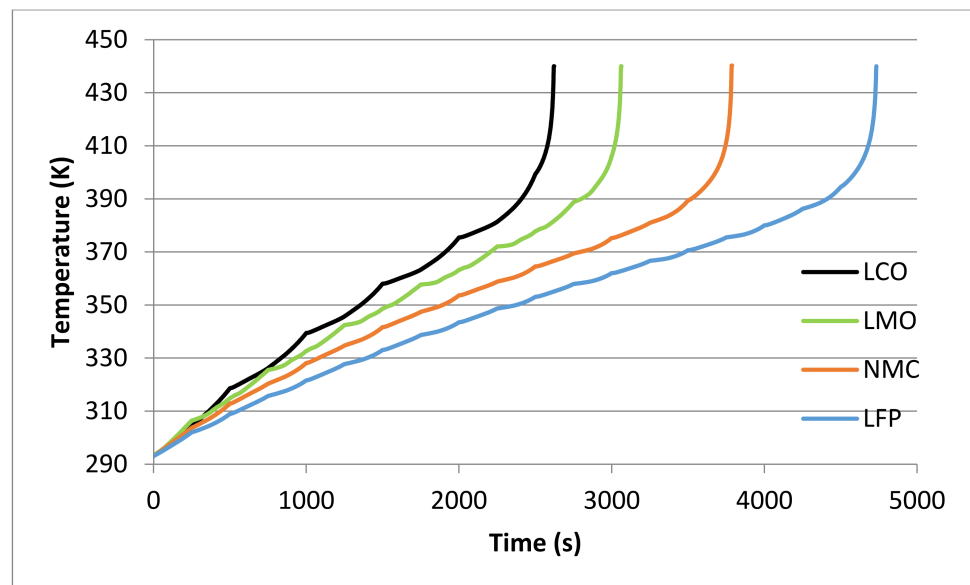


Figure 10. Temperature profiles as a function of time ($h = 4 \text{ W/m}^2\text{K}$).

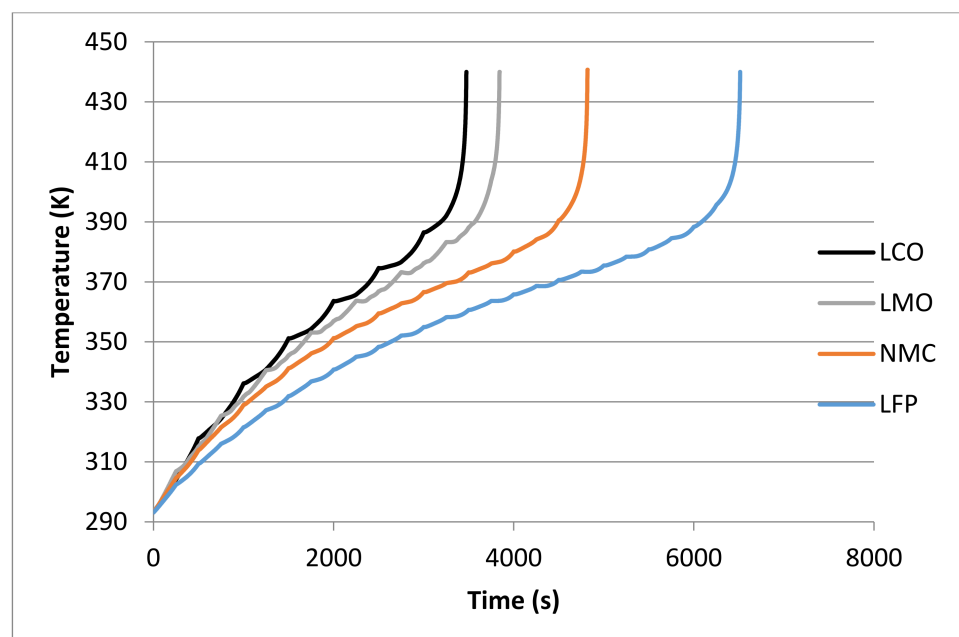


Figure 11. Temperature profiles as a function of time ($h = 6 \text{ W/m}^2\text{K}$).

As observed in the validation step (Figure 3), in addition to the heat exchange coefficient, ambient temperature also has an influence on the thermal behavior of the cell. Based on this, the thermal runaway ignition time was investigated for two additional ambient temperatures (namely, 273 and 313 K) for all chemistries. Temperature trends qualitatively similar to those reported in Figures 8–13 were obtained so that the corresponding curves are not repeated here, but the ignition times are synthetically reported altogether in Table 6.

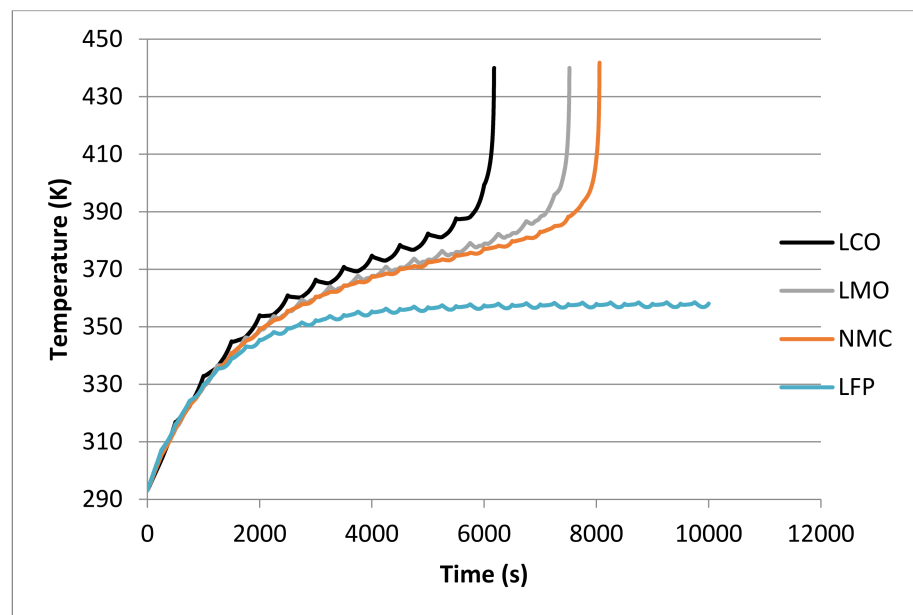


Figure 12. Temperature profiles as a function of time ($h = 8 \text{ W/m}^2\text{K}$).

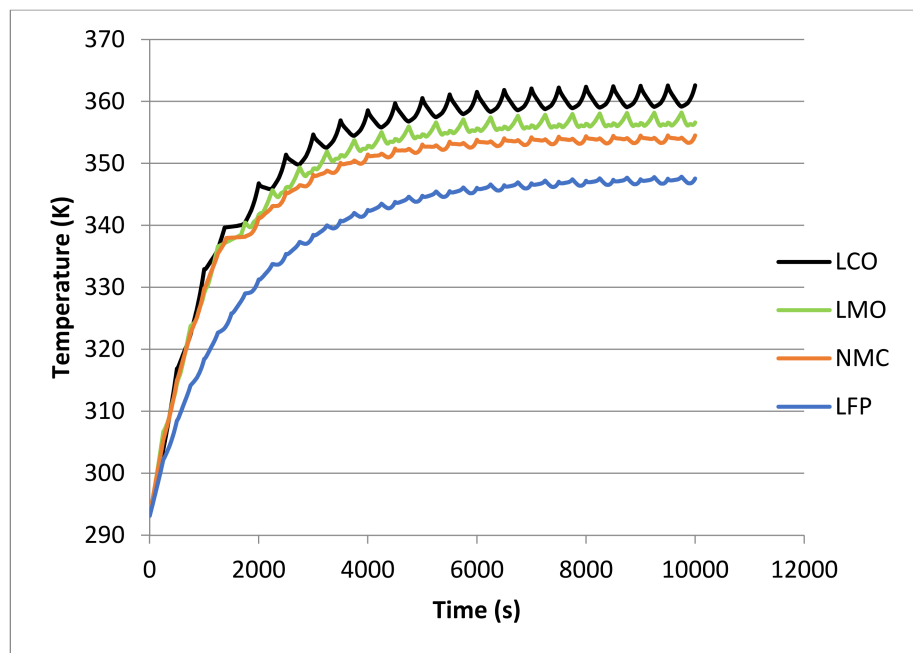


Figure 13. Temperature profiles as a function of time ($h = 10 \text{ W/m}^2\text{K}$).

As might be expected, it is apparent that a lower temperature of the external environment will improve the thermal stability of the cells [75], increasing the thermal runaway ignition time and preventing it already for $h < 8 \text{ W/m}^2\text{K}$ for all cells at 273 K (for the LFP cell, even less than $6 \text{ W/m}^2\text{K}$ is enough for a stable operation). This agrees well with the results obtained from oven tests by Lopez et al. [77] for an LCO cell.

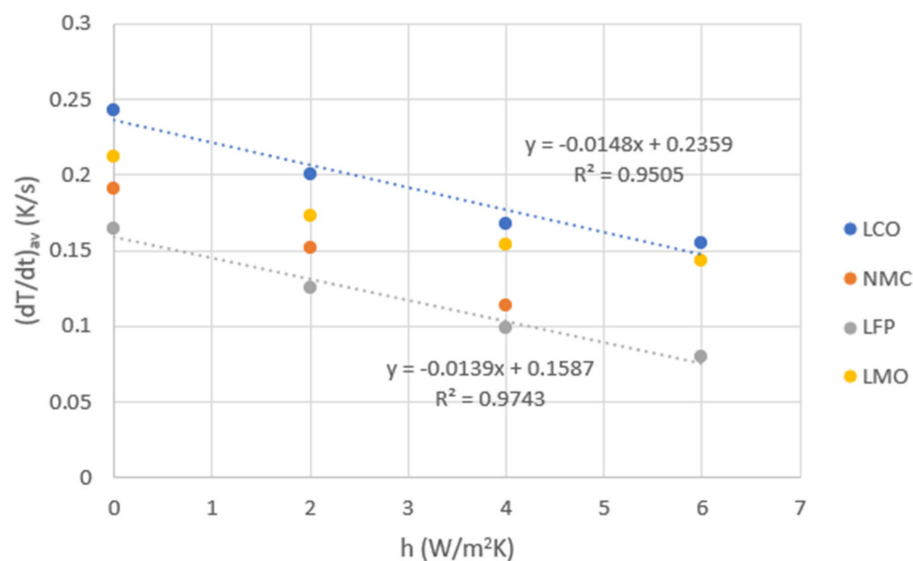


Figure 14. Heating rate as a function of h .

Table 6. Thermal runaway ignition times for all cathodes at different ambient temperatures and heat exchange conditions.

Cathode Material	Initial Temperature (K)	t_{TR} (s)					
		$h = 0 \text{ W/m}^2\text{K}$	$h = 2 \text{ W/m}^2\text{K}$	$h = 4 \text{ W/m}^2\text{K}$	$h = 6 \text{ W/m}^2\text{K}$	$h = 8 \text{ W/m}^2\text{K}$	$h = 10 \text{ W/m}^2\text{K}$
LCO	273.15	2212	2664	3407	5373		
	293.15	1892	2172	2624	3476	6179	
	313.15	1550	1760	2026	2445	3137	5379
LMO	273.15	2274	2773	3704	6443		
	293.15	2115	2579	3064	3844	7519	
	313.15	1578	1792	2083	2503	3254	5394
NMC	273.15	2313	2848	3890	7656		
	293.15	2330	2842	3788	4821	8055	
	313.15	1612	1822	2118	2585	3467	6475
LFP	273.15	2394	3078	4664			
	293.15	2859	3565	4733	6515		
	313.15	1727	2015	2346	3067	4967	

In terms of cathode chemistry, it was also found that the LFP type is characterized by a higher thermal stability; the NMC cathode also behaves rather well, while the LCO is still characterized by a higher sensitivity to temperature increases.

At any temperature, t_{TR} has an exponential-like trend (Figure 15) [75] so that beyond a given value of h its effect increases more markedly. It is hardly the case highlighting that a combination of a low temperature and a high heat transfer coefficient will provide the most beneficial conditions for a safe operation of the cells; for example, at 273 K and $h = 10 \text{ W/m}^2\text{K}$, the maximum constant value of the temperature ranges between 340 K (LCO) and 320 K (LFP).

It might be expected that a temperature gradient would establish within the cell during operation; based on this consideration and adopting a conservative approach, the maximum temperature calculated by the model was reported in the above figures. However, up to the onset of the thermal runaway, an almost homogeneous temperature distribution was actually calculated within the cell: Figure 16a,c report the internal temperature distribution within an LCO cell after one full charge–discharge cycle for $h = 0$ and $h = 10 \text{ W/m}^2\text{K}$, respectively, for the run at 313 K initial temperature.

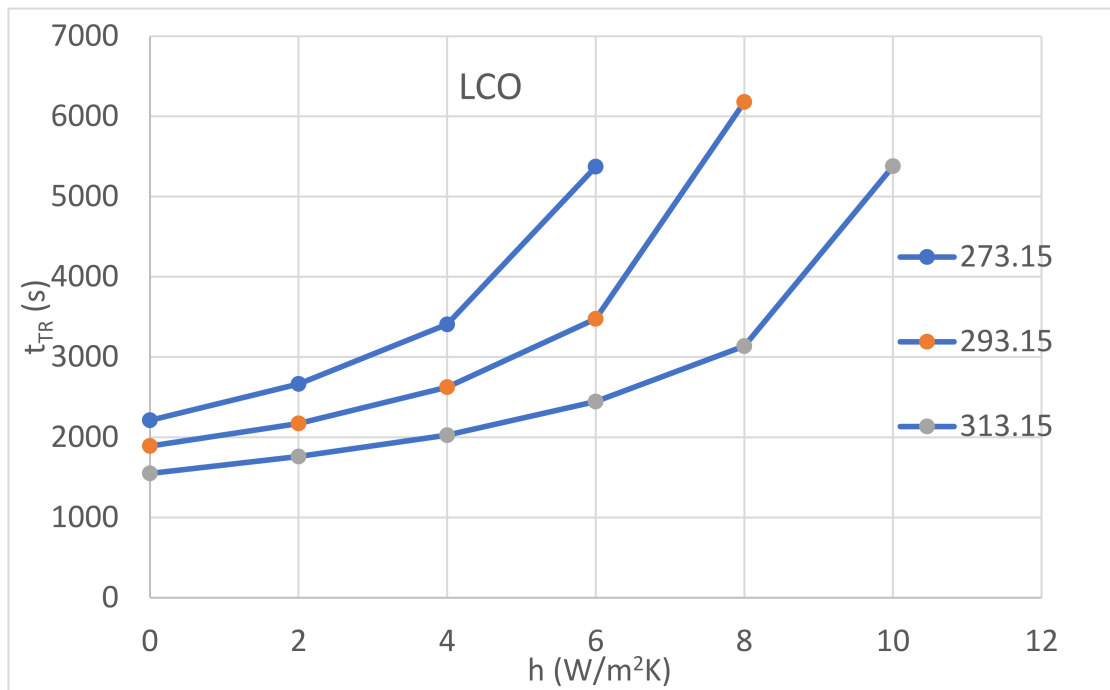


Figure 15. Thermal runaway ignition time for different ambient temperatures and heat exchange conditions (LCO cathode).

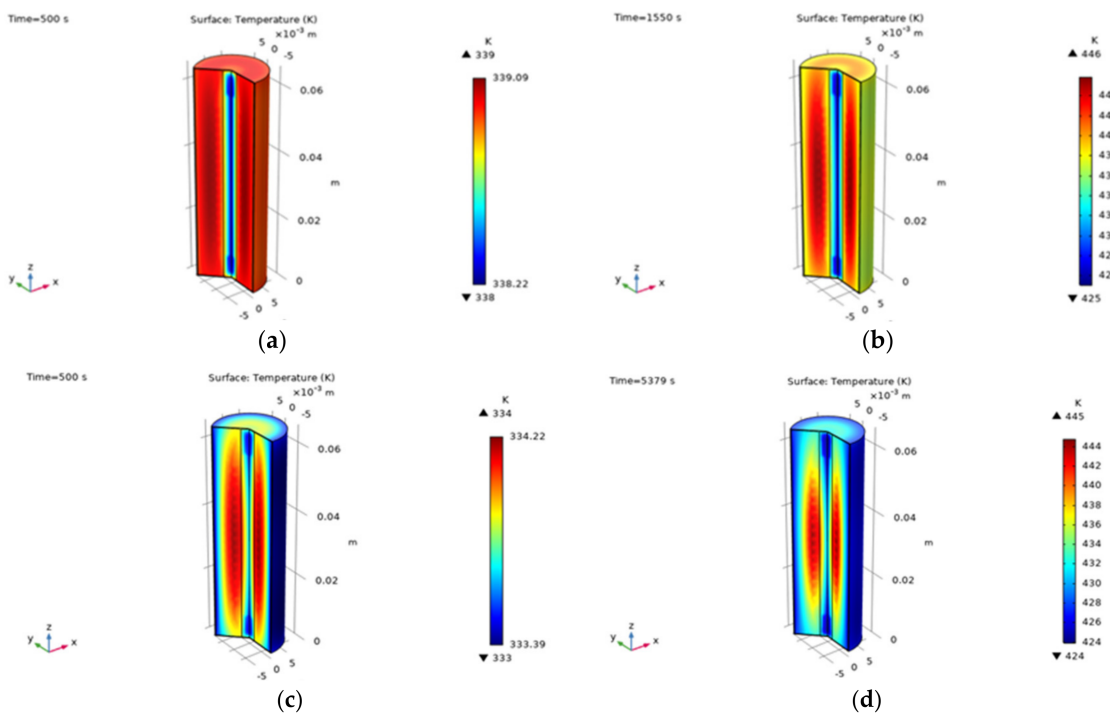


Figure 16. Thermal distribution inside an LCO cathode cell: (a) after one complete charge–discharge cycle, $h = 0 \text{ W/m}^2\text{K}$; (b) at the thermal runaway ignition time, $h = 0 \text{ W/m}^2\text{K}$; (c) after one complete charge–discharge cycle, $h = 10 \text{ W/m}^2\text{K}$; and (d) at the thermal runaway ignition time, $h = 10 \text{ W/m}^2\text{K}$. Initial $T = 313 \text{ K}$.

It can be seen that a very small temperature variation is present within the active volume of the cell, no matter where the temperature is estimated. Onda et al. [85] calculated a maximum difference between the surface temperature and that at the center of the cell of

less than 2 °C at the end of 3C discharge cycles for an LCO cell. Guo et al. [48] calculated small gradients in two directions of a prismatic LFP cell, whereas they estimated a difference of up to 30 °C between the center of the cell and its surface in the thickness direction; this was due to low thermal conductivity materials in that direction. Small variations of the internal temperature were also reported by Kim et al. [11] from simulations of a cobalt oxide cathode in an oven. Chen and Evans [12] calculated small temperature gradients also in large prismatic cells; however, Kim et al. [11] suggested that larger cells are “intrinsically more vulnerable to thermal runaway” because of their lower surface/volume ratio, “which in turn reduces cooling area per volumetric heat generation”.

It is worth highlighting here that all the above observations are applicable to “new” cells only, with optimal and constant physical properties, while due to several causes (such as aging, manufacture defects, etc.), unpredicted “hot spots” can develop within a cell, where the ignition of the thermal runaway can occur much earlier than expected and even under theoretically safe conditions [86–90].

Closer to the onset of the thermal runaway, larger temperature gradients are observed, with a variability in the order of 15–20 K in the active area (see Figure 16b,d). This finding would introduce some uncertainty in the definition of the ignition time, which would thus depend on the location of the adopted reference temperature; however, as seen above, the temperature increase in the proximity of the ignition time is so rapid that only small variations of t_{TR} would derive.

From the data reported so far, it must be highlighted that in addition to the above considerations, an efficient cooling system brings also another very important beneficial result: besides delaying or even preventing thermal runaway, in any case, an efficient cooling process will lead to a lower average temperature of the cell so that in case of an accident (e.g., due to a mechanical impact or other temperature-unrelated causes), the consequences of the failure are expected to be milder than in case of a higher energy content of the cell, associated with its higher final temperature.

4.2. Propagation

Since in most of the applications batteries are grouped into large packs, the problem of a generalized thermal runaway, originated from a single cell failure and potentially involving adjacent cells, is present [67,91]. Given the influence of the external temperature highlighted above, in the present section, the simulation of a cell exposed to the heat generated by one or more adjacent cells was investigated. In such a condition, the heat entering the cell through the external surface can be calculated as

$$Q = h \cdot (T_{\text{ext}} - T) \quad (36)$$

where T_{ext} was assumed at 420 K; T is the variable cell surface temperature, and h [$\text{W}/\text{m}^2\text{K}$] is the external heat transfer coefficient with air. Several values were assumed in the literature for the latter parameter, commonly in the range of 4–10 $\text{W}/\text{m}^2\text{K}$ [75,81], in addition to the adiabatic condition $h = 0 \text{ W}/\text{m}^2\text{K}$; however, larger ranges were also adopted [75,77]. Here, h was calculated from fundamental parameters assuming natural convection with the external air around a cylindrical cell and calculating the nondimensional parameters of interest by the conventional relations for the Rayleigh (Ra), Prandtl (Pr), and Nusselt (Nu) numbers, respectively:

$$Ra = \frac{\beta \Delta T g L^3}{\alpha \nu} \quad (37)$$

$$Pr = \frac{\nu}{\alpha} \quad (38)$$

$$Nu = \left\{ 0.825 + \frac{0.387 Ra^{1/6}}{\left[1 + \left(\frac{0.492}{Pr} \right)^{9/16} \right]^{8/27}} \right\}^2 \quad (39)$$

β is the volumetric expansion coefficient (calculated as $\beta = 1/T$ [K⁻¹] for an ideal gas); ΔT is the temperature difference between cell surface and air temperature [K]; g is the acceleration of gravity [m/s²], and L is the cell height [m]. The kinetic viscosity ν [m²/s] and the thermal diffusivity α [m²/s] of air were calculated from

$$\nu = \frac{\mu}{\rho} \quad (40)$$

$$\alpha = \frac{k}{\rho c_p} \quad (41)$$

Assuming the values reported in Table 7 for the physical parameters [92], an average value of $h = 7.5$ W/m²K was obtained, which was adopted as a reference value for the following simulations.

Table 7. Physical parameters for air at 420 K [92].

β [K ⁻¹]	2.38×10^{-3}	Volumetric expansion coefficient
L [m]	0.065	Characteristic dimension
μ [Pa·s]	2.4×10^{-5}	Viscosity
ρ [kg/m ³]	0.84	Air density
c_p [J/kgK]	827.8	Specific heat capacity
k [W/mK]	3.45×10^{-2}	Thermal conductivity

As might be expected, because of the additional source of heat from the exterior, the ignition times for the cell thermal runaway are lower than those calculated above for an isolated cell. In Figure 17, the temperature–time profiles for such a system with all cathode types are shown.

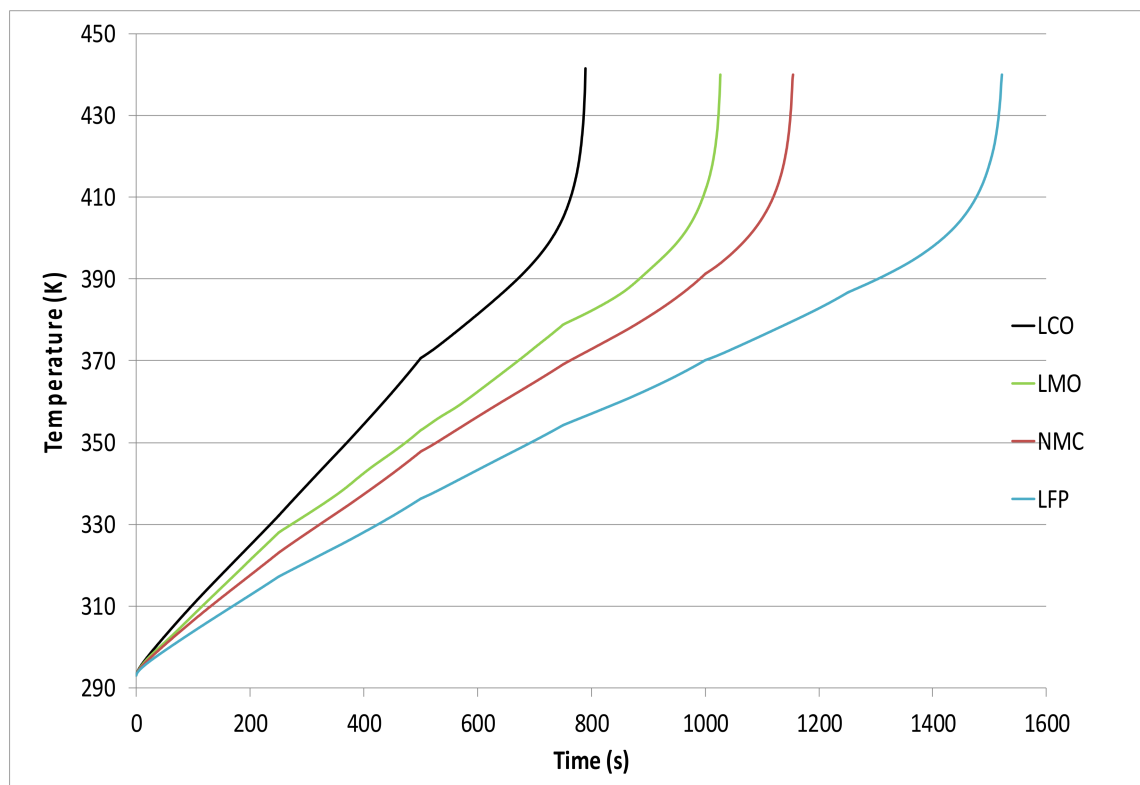


Figure 17. Temperature profile as a function of time for a cell exposed to an external thermal runaway ($T_{\text{ext}} = 420$ K; $h = 7.5$ W/m²K).

It must be observed that in real conditions, the actual ignition times can be rather different from those calculated under the ideal and simplified configuration adopted in the present study. In fact, the initial temperature of the cell can be higher than the ambient temperature, depending on the operation modality of the cell, on the service time of the pack, on the number of cycles, etc. Furthermore, the number of cells already in runaway conditions can vary so that a nonhomogeneous distribution of the temperature around the analyzed cell can be generated. As a consequence, the values presented here can be assumed only as indicative and are to be compared with the previous results for a stand-alone cell.

For a direct comparison with the previous results, the onset times for the thermal runaway of a cell under an external heat flux are synthetically reported in Table 8 for all cathode materials, along with the values obtained for an isolated cell under adiabatic conditions ($h = 0 \text{ W/m}^2\text{K}$).

Table 8. Thermal runaway ignition times for different cell materials and conditions.

Cathode Material	t_R (s)	t_R (s)
	$T_{\text{ext}} = 420 \text{ K}$, $h = 7.5 \text{ W/m}^2\text{K}$	$T_{\text{ext}} = 293 \text{ K}$, $h = 0 \text{ W/m}^2\text{K}$
LCO	790	1892
LMO	1027	2115
NMC	1154	2330
LFP	1522	2859

It can be seen that even when compared with the worst conditions previously investigated, i.e., no refrigeration with the external air in the presence of adjacent cells already under a thermal runaway, a cell will fail much more rapidly than predictable based on the internal heat generation only. In practice, once a thermal runaway has occurred in a given cell, it is likely that it will propagate to the whole pack in a short time. This conclusion is drawn on heat exchange considerations only; however, due to the consequences of the failure of a cell after a thermal runaway (i.e., a fire and/or an explosion), the propagation to the whole battery pack can occur even earlier than calculated in Table 8, thus further stressing the critical importance of thermal runaway prevention in most of the applications.

The effect of the incoming heat is apparent from Figure 18, where the temperature distribution inside a cell exposed to an external runaway, as outlined above, is reported.

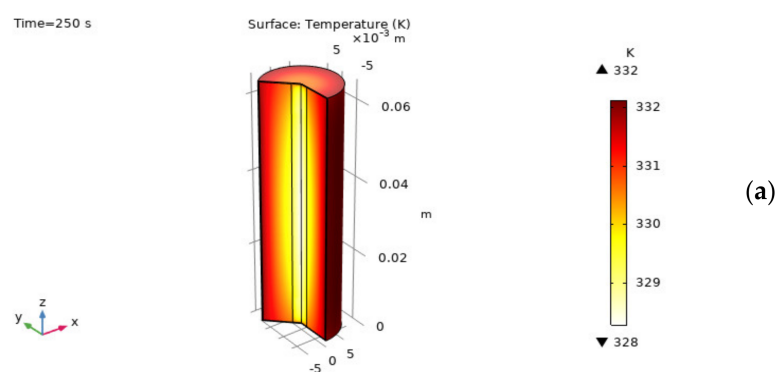


Figure 18. Cont.

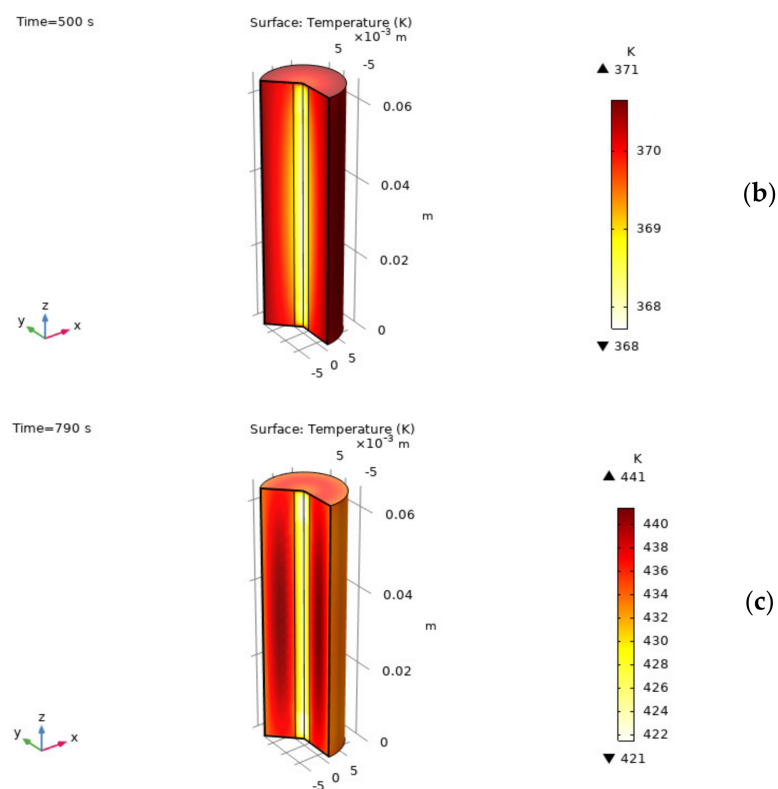


Figure 18. Temperature distribution inside an LCO cell exposed to an external heat flux: (a) at the end of the first charging phase; (b) at the end of the first full charging–discharging cycle; and (c) at the ignition time.

Initially, the external surface of the cell is warmer than its inner part because of the exposure to a hotter environment; however, once the exothermic reactions have started inside the cell, this heat becomes more significant, and hot spots are generated in the inner volume, quickly leading to its failure.

5. Conclusions

In the present paper, a simulation model was set up to investigate the onset of thermal runaway in Li-ion cells under thermal abuse and various operating conditions. The model consists of both the electrochemical and the thermal submodels of the cell, thus including the exothermic reactions at the origin of the overheating of the cell. The adoption of interconnected interfaces allowed to properly take into account the variability of the involved parameters with the temperature and to discharge some simplifying assumptions, which were often assumed in the previous literature. The model provides the significant advantage of allowing to quantitatively assess the behavior of several types of cells under abuse conditions without the need for an experimental investigation.

To summarize the present conclusions, as far as the influence of the cell structure is concerned, it was found that the presence of a lithium–iron–phosphate cathode provides the cell with higher thermal stability than that assessed with the other cathodes. Conversely, a LiCoO_2 cathode is characterized by much lower stability with the thermal runaway phenomenon occurring much earlier and for a wider range of conditions.

An efficient cooling system plays a decisive role in thermal runaway prevention, significantly increasing the operation time for all cells and making them stable beyond given values of the external heat transfer coefficient. As might be expected, the required cooling efficiency increases with decreasing intrinsic stability of the cell, and a synergic effect is also associated with the initial temperature of the cooling medium.

Based on the same considerations, it was also shown that a cell in a pack will experience thermal failure much more quickly than a single stand-alone cell if exposed to the heat flux due to the thermal runaway of one or more neighboring cells.

Author Contributions: M.C.: software, performing simulations, and validation; G.V.: resources; B.M.: methodology and supervision; R.B.: conceptualization, methodology, writing—original draft preparation, review, and editing. All authors have read and agreed to the published version of the manuscript.

Funding: This research received no external funding.

Conflicts of Interest: The authors declare no conflict of interest.

References

1. Berckmans, G.; Messagie, M.; Smekens, J.; Omar, N.; Vanhaverbeke, L.; Van Mierlo, J. Cost Projection of State of the Art Lithium-Ion Batteries for Electric Vehicles Up to 2030. *Energies* **2017**, *10*, 1314. [[CrossRef](#)]
2. Dunn, J.B.; Gaines, L.; Kelly, J.C.; James, C.; Gallagher, K.G. The significance of Li-ion batteries in electric vehicle life-cycle energy and emissions and recycling's role in its reduction. *Energy Environ. Sci.* **2015**, *8*, 158–168. [[CrossRef](#)]
3. Park, J.K. *Principles and Applications of Lithium Secondary Batteries*, 1st ed.; Wiley-VCH Verlag GmbH & Co. KGaA: Weinheim, Germany, 2012.
4. Santhanagopalan, S.; Smith, K.; Neubauer, J.; Kim, G.H.; Pesaran, A.; Keyser, M. *Design and Analysis of Large Lithium-Ion Battery Systems*; Artech House: Miami, FL, USA, 2015.
5. Feng, X.; Ouyang, M.; Liu, X.; Lu, L.; Xia, Y.; He, X. Thermal runaway mechanism of lithium ion battery for electric vehicles: A review. *Energy Storage Mater.* **2018**, *10*, 246–267. [[CrossRef](#)]
6. Wen, J.; Yu, Y.; Chen, C. A Review on Lithium-Ion Batteries Safety Issues: Existing Problems and Possible Solutions. *Mater. Express* **2012**, *2*, 197–212. [[CrossRef](#)]
7. Wang, Q.; Ping, P.; Zhao, X.; Chu, G.; Sun, J.; Chen, C. Thermal runaway caused fire and explosion of lithium ion battery. *J. Power Sources* **2012**, *208*, 210–224. [[CrossRef](#)]
8. Hendricks, C.; Williard, N.; Mathew, S.; Pecht, M. A failure modes, mechanisms, and effects analysis (FMMEA) of lithium-ion batteries. *J. Power Sources* **2015**, *297*, 113–120. [[CrossRef](#)]
9. Soares, F.J.; Carvalho, L.; Costa, I.C.; Iria, J.P.; Bodet, J.M.; Jacinto, G.; Lecocq, A.; Roessner, J.; Caillard, B.; Salvi, O. The STABALID project: Risk analysis of stationary Li-ion batteries for power system applications. *Reliab. Eng. Syst. Saf.* **2015**, *140*, 142–175. [[CrossRef](#)]
10. Bubbico, R.; Greco, V.; Menale, C. Hazardous scenarios identification for Li-ion secondary batteries. *Saf. Sci.* **2018**, *108*, 72–88. [[CrossRef](#)]
11. Kim, G.H.; Pesaran, A.; Spotnitz, R. A three-dimensional thermal abuse model for lithium-ion cells. *J. Power Sources* **2007**, *170*, 476–489. [[CrossRef](#)]
12. Chen, Y.J.W.; Evans, J.W. Thermal Analysis of Lithium-Ion Batteries. *J. Electrochem. Soc.* **1996**, *143*, 2708–2712. [[CrossRef](#)]
13. Balakrishnan, P.G.; Ramesh, R.; Prem Kumar, T. Safety mechanisms in lithium-ion batteries. *J. Power Sources* **2006**, *155*, 401–414. [[CrossRef](#)]
14. Chen, S.C.; Wan, C.C.; Wang, Y.Y. Thermal analysis of lithium-ion batteries. *J. Power Sources* **2005**, *140*, 111–124. [[CrossRef](#)]
15. Zhang, L.; Zhao, P.; Xu, M.; Wang, X. Computational identification of the safety regime of Li-ion battery thermal runaway. *Appl. Energy* **2020**, *261*, 114440. [[CrossRef](#)]
16. Mikolajczak, C.; Kahn, M.; White, K.; Long, F.T. *Lithium-Ion Batteries Hazard and Use Assessment*; Springer: New York, NY, USA, 2011.
17. Zhang, Z.J.; Ramadass, P.; Fang, W. Safety of Lithium-Ion Batteries. In *Lithium-Ion Batteries: Advances and Applications*; Pistoia, G., Ed.; Elsevier: Amsterdam, The Netherlands, 2014; pp. 409–436.
18. Kaliaperumal, M.; Dharanendrakumar, M.S.; Prasanna, S.; Abhishek, K.V.; Chidambaram, R.K.; Adams, S.; Zaghbi, K.; Reddy, M.V. Cause and Mitigation of Lithium-Ion Battery Failure—A Review. *Materials* **2021**, *14*, 5676. [[CrossRef](#)] [[PubMed](#)]
19. Xu, B.; Lee, J.; Kwon, D.; Kong, L.; Pecht, M. Mitigation strategies for Li-ion battery thermal runaway: A review. *Renew. Sustain. Energy Rev.* **2021**, *150*, 111437. [[CrossRef](#)]
20. Jeevarajan, J. Safety of commercial lithium-ion cells and batteries. In *Lithium-Ion Batteries*; Pistoia, G., Ed.; Elsevier: Amsterdam, The Netherlands, 2014; pp. 387–407.
21. Spotnitz, R.M.; Weaver, J.; Yeduvaka, G.; Doughty, D.H.; Roth, E.P. Simulation of abuse tolerance of lithium-ion battery packs. *J. Power Sources* **2007**, *163*, 1080–1086. [[CrossRef](#)]
22. Chen, Y.S.; Hu, C.C.; Li, Y.Y. The importance of heat evolution during the overcharge process and the protection mechanism of electrolyte additives for prismatic lithium ion batteries. *J. Power Sources* **2008**, *181*, 69–73. [[CrossRef](#)]
23. Kise, M.; Yoshioka, S.; Kuriki, H. Relation between composition of the positive electrode and cell performance and safety of lithium-ion PTC batteries. *J. Power Sources* **2007**, *174*, 861–866. [[CrossRef](#)]

24. Jossen, A.; Spath, V.; Doring, H.; Garche, J. Reliable battery operation—A challenge for the battery management system. *J. Power Sources* **1999**, *84*, 283–286. [[CrossRef](#)]
25. Al-Hallaj, S.; Selman, J.R. Thermal modeling of secondary lithium batteries for electric vehicle/hybrid electric vehicle applications. *J. Power Sources* **2002**, *110*, 341–348. [[CrossRef](#)]
26. Sabbah, R.; Kizilel, R.; Selman, J.R.; Al-Hallaj, S. Active (air-cooled) vs. passive (phase change material) thermal management of high power lithium-ion packs: Limitation of temperature rise and uniformity of temperature distribution. *J. Power Sources* **2008**, *182*, 630–638. [[CrossRef](#)]
27. Bubbico, R.; D’Annibale, F.; Mazzarotta, B.; Menale, C. Analysis of passive temperature control systems using PCM for application to secondary batteries cooling. *J. Thermal Sci. Eng. Appl.* **2018**, *10*, 061009. [[CrossRef](#)]
28. Claus, D.; Besenhard, J.O. *Handbook of Battery Materials*; Wiley-VCH: Weinheim, Germany, 2011.
29. Yuan, X.; Liu, H.; Zhang, J. *Lithium-Ion Batteries Advanced Materials and Technologies*; CRC Press, Taylor & Francis Group: Boca Raton, FL, USA, 2011.
30. Nitta, N.; Wu, F.; Lee, J.T.; Yushin, G. Li-ion battery materials: Present and future. *Mater. Today* **2015**, *5*, 252–264. [[CrossRef](#)]
31. Goodenough, J.B.; Kim, Y. Challenges for Rechargeable Li Batteries. *Chem. Mater.* **2010**, *22*, 587–603. [[CrossRef](#)]
32. Hatchard, T.D.; MacNeil, D.D.; Basu, A.; Dahn, J.R. Thermal Model of Cylindrical and Prismatic Lithium-Ion Cells. *J. Electrochem. Soc.* **2001**, *148*, A755. [[CrossRef](#)]
33. Abraham, D.P.; Roth, E.P.; KostECKI, R.; McCarthy, K.; MacLaren, S.; Doughty, D.H. Diagnostic examination of thermally abused high-power lithium-ion cells. *J. Power Sources* **2006**, *161*, 648–657. [[CrossRef](#)]
34. Maleki, H.; Howard, J.N. Role of the cathode and anode in heat generation of Li-ion cells as a function of state of charge. *J. Power Sources* **2004**, *137*, 117–127. [[CrossRef](#)]
35. Zeng, Y.; Wu, K.; Wang, D.; Wang, Z.; Chen, L. Overcharge investigation of lithium-ion polymer batteries. *J. Power Sources* **2006**, *160*, 1302–1307. [[CrossRef](#)]
36. Waag, W.; Käbitz, S.; Sauer, D.U. Experimental investigation of the lithium-ion battery impedance characteristic at various conditions and aging states and its influence on the application. *Appl. Energy* **2013**, *102*, 885–897. [[CrossRef](#)]
37. Roth, E.P.; Doughty, D.H.; Franklin, J. DSC investigation of exothermic reactions occurring at elevated temperatures in lithium-ion anodes containing PVDF-based binders. *J. Power Sources* **2004**, *134*, 222–234. [[CrossRef](#)]
38. Kawamura, T.; Kimura, A.; Egashira, M.; Okada, S.; Yamaki, J.-I. Thermal stability of alkyl carbonate mixed-solvent electrolytes for lithium ion cells. *J. Power Sources* **2002**, *104*, 260–264. [[CrossRef](#)]
39. Maleki, H.; Deng, G.; Anani, A.; Howard, J. Thermal Stability Studies of Li-Ion Cells and Components. *J. Electrochem. Soc.* **1999**, *146*, 3224–3229. [[CrossRef](#)]
40. Forgez, C.; Do, D.V.; Friedrich, G.; Morcrette, M.; Delacourt, C. Thermal modeling of a cylindrical LiFePO₄/graphite lithium-ion battery. *J. Power Sources* **2010**, *195*, 2961–2968. [[CrossRef](#)]
41. Wang, Q.S.; Sun, J.H.; Chen, X.F.; Chu, G.Q.; Chen, C.H. Effects of solvents and salt on the thermal stability of charged LiCoO₂. *Mater. Res. Bull.* **2009**, *44*, 543–548. [[CrossRef](#)]
42. Watanabe, I.; Yamaki, J. Thermalgravimetry–mass spectrometry studies on the thermal stability of graphite anodes with electrolyte in lithium-ion battery. *J. Power Sources* **2006**, *153*, 402–404. [[CrossRef](#)]
43. Yang, H.; Shen, X.D. Dynamic TGA–FTIR studies on the thermal stability of lithium/graphite with electrolyte in lithium-ion cell. *J. Power Sources* **2007**, *167*, 515–519. [[CrossRef](#)]
44. Pasquier, A.D.; Disma, F.; Bowmer, T.; Gozdz, A.S.; Amatucci, G.; Tarascon, J.M. Differential Scanning Calorimetry Study of the Reactivity of Carbon Anodes in Plastic Li-Ion Batteries. *J. Electrochem. Soc.* **1998**, *145*, 472–477. [[CrossRef](#)]
45. Orendorff, C.J.; Roth, E.P.; Nagasubramanian, G. Experimental triggers for internal short circuits in lithium-ion cells. *J. Power Sources* **2011**, *196*, 6554–6558. [[CrossRef](#)]
46. Leising, R.A.; Palazzo, M.J.; Takeuchi, E.S.; Takeuchi, K.J. Abuse Testing of Lithium-Ion Batteries: Characterization of the Overcharge Reaction of LiCoO₂/Graphite Cells. *J. Electrochem. Soc.* **2001**, *148*, A838–A844. [[CrossRef](#)]
47. Ohsaki, T.; Kishi, T.; Kuboki, T.; Takami, N.; Shimura, N.; Sato, Y.; Sekino, M.; Satoh, A. Overcharge reaction of lithium-ion batteries. *J. Power Sources* **2005**, *146*, 97–100. [[CrossRef](#)]
48. Guo, G.; Long, B.; Cheng, B.; Zhou, S.; Xu, P.; Cao, B. Three-dimensional thermal finite element modeling of lithium-ion battery in thermal abuse application. Three-dimensional thermal finite element modeling of lithium-ion battery in thermal abuse application. *J. Power Sources* **2010**, *195*, 2393–2398. [[CrossRef](#)]
49. Chen, S.C.; Wang, Y.Y.; Wan, C.C. Thermal Analysis of Spirally Wound Lithium Batteries. *J. Electrochem. Soc.* **2006**, *153*, A637–A648. [[CrossRef](#)]
50. Freitas, G.C.S.; Peixoto, F.C.; Vianna, A.S. Simulation of a thermal battery using Phoenix[®]. *J. Power Sources* **2008**, *179*, 424–429. [[CrossRef](#)]
51. Zhang, X.W. Thermal analysis of a cylindrical lithium-ion battery. *Electrochim. Acta* **2011**, *56*, 1246–1255. [[CrossRef](#)]
52. Jeon, D.H.; Baek, S.M. Thermal modeling of cylindrical lithium ion battery during discharge cycle. *Energy Convers. Manag.* **2011**, *52*, 2973–2981. [[CrossRef](#)]
53. Kim, U.S.; Yi, J.; Shin, C.B.; Han, T.; Park, S. Modelling the thermal behaviour of a lithium-ion battery during charge. *J. Power Sources* **2011**, *196*, 5115–5121. [[CrossRef](#)]
54. Spotnitz, R.; Franklin, J. Abuse behavior of high-power, lithium-ion cells. *J. Power Sources* **2003**, *113*, 81–100. [[CrossRef](#)]

55. Bharathy, S.; Parimalam, A.D.; MacIntosh, R.; Brett, L. Lucht, Decomposition Reactions of Anode Solid Electrolyte Interphase (SEI) Components with LiPF₆. *J. Phys. Chem. C* **2017**, *121*, 22733–22738.
56. Kriston, A.; Adanouj, I.; Ruiz, V.; Pfrang, A. Quantification and simulation of thermal decomposition reactions of Li-ion battery materials by simultaneous thermal analysis coupled with gas analysis. *J. Power Sources* **2019**, *435*, 226774. [[CrossRef](#)]
57. Wang, Q.S.; Sun, J.H.; Yao, X.L.; Chen, C.H. Thermal Behavior of Lithiated Graphite with Electrolyte in Lithium-Ion Batteries. *J. Electrochem. Soc.* **2006**, *153*, A329–A333. [[CrossRef](#)]
58. Shigematsu, Y.; Ue, M.; Yamaki, J. Thermal Behavior of Charged Graphite and Li_xCoO₂ in Electrolytes Containing Alkyl Phosphate for Lithium-Ion Cells. *J. Electrochem. Soc.* **2009**, *156*, A176–A180. [[CrossRef](#)]
59. Lee, S.Y.; Kim, S.K.; Ahn, S. Performances and thermal stability of LiCoO₂ cathodes encapsulated by a new gel polymer electrolyte. *J. Power Sources* **2007**, *174*, 480–483. [[CrossRef](#)]
60. COMSOL. Batteries & Fuel Cells Module Application Library Manual. © 1998–2016 COMSOL.
61. COMSOL. Batteries & Fuel Cells Module User's Guide. © 1998–2018 COMSOL.
62. Hu, X.; Liu, W.; Lin, X.; Xie, Y. A Comparative Study of Control-Oriented Thermal Models for Cylindrical Li-Ion Batteries. *IEEE Trans. Transp. Electrification* **2019**, *5*, 1237–1253. [[CrossRef](#)]
63. Cai, L.; White, R.E. An Efficient Electrochemical–Thermal Model for a Lithium-Ion Cell by Using the Proper Orthogonal Decomposition Method. *J. Electrochem. Soc.* **2010**, *157*, A1188–A1195. [[CrossRef](#)]
64. Santhanagopalan, S.; Guo, Q.Z.; Ramadass, P.; White, R.E. Review of models for predicting the cycling performance of lithium ion batteries. *J. Power Sources* **2006**, *156*, 620–628. [[CrossRef](#)]
65. Smith, K.; Wang, C.Y. Power and thermal characterization of a lithium-ion battery pack for hybrid-electric vehicles. *J. Power Sources* **2006**, *160*, 662–673. [[CrossRef](#)]
66. Moya, A.A.; Castilla, J.; Horno, J. Ionic Transport in Electrochemical Cells Including Electrical Double-Layer Effects. A Network Thermodynamics Approach. *J. Phys. Chem.* **1995**, *99*, 1292–1298. [[CrossRef](#)]
67. Smith, K.; Kim, G.-H.; Darcy, E.; Pesaran, A. Thermal/electrical modeling for abuse-tolerant design of lithium ion modules. *Int. J. Energy Res.* **2010**, *34*, 204–215. [[CrossRef](#)]
68. Guo, M.; White, R.E. A distributed thermal model for a Li-ion electrode plate pair. *J. Power Sources* **2013**, *221*, 334–344. [[CrossRef](#)]
69. Christensen, J.; Cook, D.; Albertus, P. An Efficient Parallelizable 3D Thermochemical Model of a Li-Ion Cell. *J. Electrochem. Soc.* **2013**, *160*, A2258–A2267. [[CrossRef](#)]
70. Allu, S.; Kalnaus, S.; Elwasif, W.; Simunovic, S.; Turner, J.A.; Pannala, S. A new open computational framework for highly-resolved coupled three-dimensional multiphysics simulations of Li-ion cells. *J. Power Sources* **2014**, *246*, 876–886. [[CrossRef](#)]
71. Baba, N.; Yoshida, H.; Nagaoka, M.; Okuda, C.; Kawauchi, S. Numerical simulation of thermal behavior of lithium-ion secondary batteries using the enhanced single particle model. *J. Power Sources* **2014**, *252*, 214–228. [[CrossRef](#)]
72. Lee, K.-J.; Smith, K.; Pesaran, A.; Kim, G.-H. Three dimensional thermal-, electrical-, and electrochemical-coupled model for cylindrical wound large format lithium-ion batteries. *J. Power Sources* **2013**, *241*, 20–32. [[CrossRef](#)]
73. Al Hallaj, S.; Maleki, H.; Hong, J.S.; Selman, J.R. Thermal modeling and design considerations of lithium-ion batteries. *J. Power Sources* **1999**, *83*, 1–8. [[CrossRef](#)]
74. Kim, U.S.; Shin, C.B.; Kim, C.S. Effect of electrode configuration on the thermal behavior of a lithium-polymer battery. *J. Power Sources* **2008**, *180*, 909–916. [[CrossRef](#)]
75. Melcher, A.; Ziebert, C.; Rohde, M.; Seifert, H.J. Modeling and Simulation of the Thermal Runaway Behavior Li-Ion Cells-Computing of Critical Parameters. *Energies* **2016**, *9*, 292. [[CrossRef](#)]
76. Melcher, A.; Ziebert, C.; Lei, B.; Zhao, W.; Luo, J.; Rohde, M.; Seifert, H.J. Modeling and Simulation of the Thermal Runaway in Cylindrical 18650 Lithium-Ion Batteries. In Proceedings of the 2016 COMSOL Conference, Munich, Germany, 12–14 October 2016.
77. Lopez, C.F.; Jeevarajan, J.A.; Mukherjee, P.P. Mukherjee, Characterization of Lithium-Ion Battery Thermal Abuse Behavior Using Experimental and Computational Analysis. *J. Electrochem. Soc.* **2015**, *162*, A2163–A2173. [[CrossRef](#)]
78. Xu, J.; Hendricks, C. A multiphysics Simulation of thermal Runaway in Large-Format Lithium-ion Batteries. In Proceedings of the 18th IEEE ITherm Conference, Las Vegas, NV, USA, 28–31 May 2019.
79. Frank-Kamenetskij, D.A. *Diffusion and Heat Transfer in Chemical Kinetics*; Plenum Press: New York, NY, USA, 1969.
80. Roetzel, W.; Spang, B. C3 Typical Values of Overall Heat Transfer Coefficients. In *VDI Heat Atlas*; Springer: Berlin/Heidelberg, Germany, 2010.
81. Huo, Y.; Rao, Z.; Liu, X.; Zhao, J. Investigation of power battery thermal management by using mini-channel cold plate. *Energy Convers. Manag.* **2015**, *89*, 387–395. [[CrossRef](#)]
82. Fouchard, D.; Xie, L.; Ebner, W.; Megahed, S.A. *Rechargeable Lithium and Lithium Ion (RCT) Batteries*; PV, 94-28; Megahed, S.A., Ed.; Electrochemical Society: Miami Beach, FL, USA, 1994.
83. Mendoza-Hernandez, O.S.; Ishikawa, H.; Nishikawa, Y.; Maruyama, Y.; Umeda, M. Cathode material comparison of thermal runaway behavior of Li-ion cells at different state of charges including over charge. *J. Power Sources* **2015**, *280*, 499–504. [[CrossRef](#)]
84. Jiang, J.; Dahn, J.R. ARC studies of the thermal stability of three different cathode materials: LiCoO₂; Li[Ni_{0.1}Co_{0.8}Mn_{0.1}]O₂; and LiFePO₄, in LiPF₆ and LiBoB EC/DEC electrolytes. *Electrochem. Commun.* **2004**, *6*, 39–43. [[CrossRef](#)]
85. Onda, K.; Ohshima, T.; Nakayama, M.; Fukuda, K.; Araki, T. Thermal behavior of small lithium-ion battery during rapid charge and discharge cycles. *J. Power Sources* **2006**, *158*, 535–542. [[CrossRef](#)]

86. Vetter, J.; Novák, P.; Wagner, M.R.; Veit, C.; Möller, K.C.; Besenhard, J.O.; Winter, M.; Wohlfahrt-Mehrens, M.; Vogler, C.; Hammouche, A. Ageing mechanisms in lithium-ion batteries. *J. Power Sources* **2005**, *147*, 269–281. [[CrossRef](#)]
87. Wu, C.; Zhu, C.; Ge, Y.; Zhao, Y. A Review on Fault Mechanism and Diagnosis Approach for Li-Ion Batteries. *J. Nanomater.* **2015**, *2015*, 9. [[CrossRef](#)]
88. Menale, C.; D'Annibale, F.; Mazzarotta, B.; Bubbico, R. Thermal management of lithium-ion batteries: An experimental investigation. *Energy* **2019**, *182*, 57–71. [[CrossRef](#)]
89. Wang, Y.; Yan, X.; Bie, X.; Fu, Q.; Du, F.; Chen, G.; Wang, C.; Wei, Y. Effects of Aging in Electrolyte on the Structural and Electrochemical Properties of the $\text{Li}[\text{Li}_{0.18}\text{Ni}_{0.15}\text{Co}_{0.15}\text{Mn}_{0.52}]\text{O}_2$ Cathode Material. *Electrochim. Acta* **2014**, *116*, 250–257. [[CrossRef](#)]
90. Bodenes, L.; Naturel, R.; Martinez, H.; Dedryvère, R.; Menetrier, M.; Croguennec, L.; Pérès, J.P.; Tessier, C.; Fischer, F. Lithium secondary batteries working at very high temperature: Capacity fade and understanding of aging mechanisms. *J. Power Sources* **2013**, *236*, 265–275. [[CrossRef](#)]
91. Abada, S.; Marlair, G.; Lecocq, A.; Petit, M.; Sauvart-Moynot, V.; Huet, F. Safety focused modeling of lithium-ion batteries: A review. *J. Power Sources* **2016**, *306*, 178–192. [[CrossRef](#)]
92. Green, D.V.; Perry, R.H. *Perry's Chemical Engineers' Handbook*, 8th ed.; McGraw-Hill Professional Publishing: Blacklick, OH, USA, 2007.